



HAL
open science

Lifetime measurements in $^{52,54}\text{Ti}$ to study shell evolution toward $N = 32$

A. Goldkuhle, C. Fransen, A. Blazhev, M. Beckers, B. Birkenbach, T. Braunroth, E. Clément, A. Dewald, J. Dudouet, J. Eberth, et al.

► To cite this version:

A. Goldkuhle, C. Fransen, A. Blazhev, M. Beckers, B. Birkenbach, et al.. Lifetime measurements in $^{52,54}\text{Ti}$ to study shell evolution toward $N = 32$. Phys.Rev.C, 2019, 100 (5), pp.054317. 10.1103/PhysRevC.100.054317. hal-02381948

HAL Id: hal-02381948

<https://hal.science/hal-02381948>

Submitted on 10 Nov 2020

HAL is a multi-disciplinary open access archive for the deposit and dissemination of scientific research documents, whether they are published or not. The documents may come from teaching and research institutions in France or abroad, or from public or private research centers.

L'archive ouverte pluridisciplinaire **HAL**, est destinée au dépôt et à la diffusion de documents scientifiques de niveau recherche, publiés ou non, émanant des établissements d'enseignement et de recherche français ou étrangers, des laboratoires publics ou privés.

Lifetime measurements in $^{52,54}\text{Ti}$ to study shell evolution toward $N = 32$

A. Goldkuhle,^{1,*} C. Fransen,¹ A. Blazhev,¹ M. Beckers,¹ B. Birkenbach,¹ T. Braunroth,¹ E. Clément,² A. Dewald,¹ J. Dudouet,³ J. Eberth,¹ H. Hess,¹ B. Jacquot,² J. Jolie,¹ Y.-H. Kim,⁴ A. Lemasson,² S. M. Lenzi,^{5,6} H. J. Li,² J. Litzinger,¹ C. Michelagnoli,^{5,6,2} C. Müller-Gatermann,¹ B. S. Nara Singh,^{7,8} R. M. Pérez-Vidal,⁹ D. Ralet,^{10,11,12} P. Reiter,¹ A. Vogt,¹ N. Warr,¹ K. O. Zell,¹ A. Ataç,¹³ D. Barrientos,¹⁴ C. Barthe-Dejean,² G. Benzoni,¹⁵ A. J. Boston,¹⁶ H. C. Boston,¹⁶ P. Bourgault,² I. Burrows,¹⁷ J. Caccitti,² B. Cederwall,¹³ M. Ciemala,¹⁸ D. M. Cullen,⁷ G. De France,² C. Domingo-Pardo,⁹ J.-L. Foucher,² G. Fremont,² A. Gadea,⁹ P. Gangnant,² V. González,¹⁹ J. Goupil,² C. Henrich,¹² C. Houarner,² M. Jean,² D. S. Judson,¹⁶ A. Korichi,¹⁰ W. Korten,²⁰ M. Labiche,¹⁷ A. Lefevre,² L. Legeard,² F. Legrue,² S. Leoni,^{15,21} J. Ljungvall,¹⁰ A. Maj,¹⁸ C. Maugeais,² L. Ménager,² N. Ménard,² R. Menegazzo,⁵ D. Mengoni,^{5,6} B. Million,¹⁵ H. Munoz,² D. R. Napoli,²² A. Navin,² J. Nyberg,²³ M. Ozille,² Zs. Podolyak,²⁴ A. Pullia,^{15,25} B. Raine,² F. Recchia,^{5,6} J. Ropert,² F. Saillant,² M. D. Salsac,²⁰ E. Sanchis,¹⁹ C. Schmitt,² J. Simpson,¹⁷ C. Spitaels,² O. Stezowski,³ Ch. Theisen,²⁰ M. Toulemonde,²⁶ M. Tripon,² J.-J. Valiente Dobón,²² G. Voltolini,² and M. Zielińska²⁰

(AGATA Collaboration)

¹*Institut für Kernphysik, Universität zu Köln, 50937 Köln, Germany*

²*GANIL, CEA/DRF-CNRS/IN2P3, BP 55027, 14076 Caen Cedex 05, France*

³*Université de Lyon, CNRS/IN2P3, IPN-Lyon, F-69622 Villeurbanne, France*

⁴*Institut Laue-Langevin, BP 156, 38042 Grenoble Cedex 9, France*

⁵*INFN Sezione di Padova, I-35131 Padova, Italy*

⁶*Dipartimento di Fisica e Astronomia dell'Università di Padova, I-35131 Padova, Italy*

⁷*Nuclear Physics Group, Schuster Laboratory, University of Manchester, Manchester, M13 9PL, United Kingdom*

⁸*School of Computing Engineering and Physical Sciences, University of the West of Scotland, Paisley, PA1 2BE, United Kingdom*

⁹*Instituto de Fisica Corpuscular, CSIC-Universidad de Valencia, E-46071 Valencia, Spain*

¹⁰*Centre de Spectrométrie Nucléaire et de Spectrométrie de Masse - CSNSM, CNRS/IN2P3 and Université Paris-Sud, F-91405 Orsay Campus, France*

¹¹*GSI, Helmholtzzentrum für Schwerionenforschung GmbH, 64291 Darmstadt, Germany*

¹²*Institut für Kernphysik, Technische Universität Darmstadt, 64289 Darmstadt, Germany*

¹³*Department of Physics, Royal Institute of Technology, SE-10691 Stockholm, Sweden*

¹⁴*CERN, CH-1211 Geneva 23, Switzerland*

¹⁵*INFN Sezione di Milano, I-20133 Milano, Italy*

¹⁶*Oliver Lodge Laboratory, The University of Liverpool, Liverpool, L69 7ZE, United Kingdom*

¹⁷*STFC Daresbury Laboratory, Daresbury, Warrington WA4 4AD, United Kingdom*

¹⁸*The Henryk Niewodniczański Institute of Nuclear Physics, Polish Academy of Sciences, ul. Radzikowskiego 152, 31-342 Kraków, Poland*

¹⁹*Departamento de Ingeniería Electrónica, Universitat de Valencia, Burjassot, Valencia, Spain*

²⁰*Irfu, CEA, Université Paris-Saclay, F-91191 Gif-sur-Yvette, France*

²¹*Dipartimento di Fisica, Università di Milano, I-20133 Milano, Italy*

²²*Laboratori Nazionali di Legnaro, INFN, I-35020 Legnaro, Italy*

²³*Department of Physics and Astronomy, Uppsala University, SE-75120 Uppsala, Sweden*

²⁴*Department of Physics, University of Surrey, Guildford, GU2 7XH, United Kingdom*

²⁵*University of Milano, Department of Physics, I-20133 Milano, Italy*

²⁶*CIMAP-GANIL (CEA-CNRS-ENSICAEN-Université de Caen), BP 5133, 14070 Caen, France*



(Received 22 August 2019; published 18 November 2019)

Lifetimes of the excited states in the neutron-rich $^{52,54}\text{Ti}$ nuclei, produced in a multinucleon-transfer reaction, were measured by employing the Cologne plunger device and the recoil-distance Doppler-shift method. The experiment was performed at the Grand Accélérateur National d'Ions Lourds facility by using the Advanced Gamma Tracking Array for the γ -ray detection, coupled to the large-acceptance variable mode spectrometer for an event-by-event particle identification. A comparison between the transition probabilities obtained from the measured lifetimes of the 2_1^+ to 8_1^+ yrast states in $^{52,54}\text{Ti}$ and that from the shell-model calculations based on the

*Corresponding author: agoldkuhle@ikp.uni-koeln.de

well-established GXPF1A, GXPF1B, and KB3G *fp* shell interactions support the $N = 32$ subshell closure. The $B(E2)$ values for ^{52}Ti determined in this work are in disagreement with the known data, but are consistent with the predictions of the shell-model calculations and reduce the previously observed pronounced staggering across the even-even titanium isotopes.

DOI: [10.1103/PhysRevC.100.054317](https://doi.org/10.1103/PhysRevC.100.054317)

I. INTRODUCTION

Understanding the evolution of shell structure toward the drip lines is one of the driving forces for many theoretical and experimental efforts, as investigations have shown that the shell structure often changes significantly as a result of the rearrangement of single-particle levels in exotic nuclear regions [1]. In this context, the $N = 40$ island of inversion represents a rich testing ground. For example, while ^{68}Ni shows doubly shell-closure character, an increase in collectivity is apparent both from excitation energies and transition strengths in the neutron-rich $^{58-66}\text{Cr}$ [2–5] and $^{62-70}\text{Fe}$ [5–8] nuclei close to the $Z = 28$ shell closure. The experimental data assisted a comprehensive description of these nuclei with respect to the high collectivity predicted using the modern shell-model calculations [2,6].

Studies of neutron-rich Ti isotopes are also essential for an understanding of the shell structure in the Ti-Cr-Fe region beyond $N = 28$ and toward $Z = 20$. Known $B(E2, 2_1^+ \rightarrow 0_{gs}^+)$ transition probabilities in ^{54}Ti [9], ^{56}Cr [10,11], ^{58}Fe [12], and ^{60}Ni [13] isotones, which in a shell-model framework can be viewed as having a completely filled valence $\nu 2p_{3/2}$ orbital, suggest a phase transition. In particular, the collective structure in ^{58}Fe evolves to a neutron-subshell closure along the isotonic chain with decreasing proton number, i.e., from ^{56}Cr over ^{54}Ti to ^{52}Ca . This observation is supported by an increased staggering of the 2_1^+ level energies for decreasing proton number as shown in Fig. 1. At the neutron shell closure $N = 28$, the isotones show a local rise in the 2_1^+ state energy but at $N = 32$ a different behavior is observed: only ^{52}Ca , ^{54}Ti , and ^{56}Cr exhibit a local increase in the 2_1^+ energy. The corresponding $B(E2; 2_1^+ \rightarrow 0_{gs}^+)$ values suggest a weak and very localized subshell closure at $N = 32$ [14–16] for the Ca, Ti, and Cr isotones, which collapses for Fe and Ni. This behavior was investigated in several recent experiments on $^{52,54,56}\text{Ti}$ and ^{58}Cr using deep-inelastic reactions [17,18], β decay [16,19], as well as Coulomb excitation at intermediate energies [9]. Essentially, all the experimental and theoretical works indicate the subshell closure at $N = 32$ is weaker compared to that at $N = 28$.

A possible explanation could be an effect similar to that for $N = 40$ isotones described in works of Otsuka *et al.* [20–22], where the proton-neutron tensor force contribution to the monopole component of the residual interaction was proposed as one of the driving factors behind the shell evolution at $N = 40$. This ensures that the $N = 40$ gap is reduced by removing protons from the $\pi 1f_{7/2}$ subshell. For nuclei close to $N = 32$, a similar effect could result in a reverse order of the $\nu 1f_{5/2}$ and $\nu 2p_{1/2}$ orbitals and is assumed to open up the shell gap at $N = 32$, i.e., the energy difference between the $\nu 2p_{3/2}$ and $(\nu 2p_{1/2}, \nu 1f_{5/2})$ orbitals with decreasing proton number from $Z = 28$ to $Z = 20$ [14].

For a better understanding of the shell evolution, data on $E2$ transition strengths between higher-spin states in ^{54}Ti ($N = 32$) are essential, which are not available to date. Furthermore, the shell-model predictions so far do not agree with the $B(E2)$ data of the neighboring ^{52}Ti that is only two neutrons away but exhibits different $B(E2)$ behavior as a function of spin to that of ^{50}Ti and ^{54}Ti , e.g., ^{52}Ti has relatively high $B(E2; 2_1^+ \rightarrow 0_{gs}^+)$ and $B(E2; 6_1^+ \rightarrow 4_1^+)$ values but a low $B(E2; 4_1^+ \rightarrow 2_1^+)$ value. In contrast, experimental (theoretical) results for ^{50}Ti (^{54}Ti) show relatively high $B(E2)$ values for the $2_1^+ \rightarrow 0_{gs}^+$ and $4_1^+ \rightarrow 2_1^+$ transitions and a low $B(E2)$ value for the $6_1^+ \rightarrow 4_1^+$ transition. So far, no successful shell-model description could be reached for ^{52}Ti , motivating a new detailed investigation of $^{52,54}\text{Ti}$ in order to obtain a comprehensive picture of the evolving shell structure with regard to the emergence of a $N = 32$ subshell closure for $Z < 26$.

In this work, the evolution of the shell structure in $^{52,54}\text{Ti}$ is studied by measuring the lifetimes of the first 2_1^+ , 4_1^+ , 6_1^+ , and 8_1^+ states in the yrast band by employing the recoil-distance Doppler-shift (RDDS) method [23]. The deduced $E2$ transition strengths are discussed together with the state-of-the-art shell-model calculations.

II. EXPERIMENTAL SETUP

The experiment was performed at the Grand Accélérateur National d'Ions Lourds (GANIL) in Caen, France using the Cologne plunger for deep-inelastic reactions [23]. The $^{52,54}\text{Ti}$ nuclei were produced via two-neutron and four-neutron multinucleon-transfer reactions induced by a ^{238}U beam at an energy of $E(^{238}\text{U}) = 1608.9$ MeV (6.76 MeV/u) impinging on a ^{50}Ti target. The target was ≈ 1.5 mg/cm² thick and had a $^{\text{nat}}\text{Cu}$ layer of ≈ 0.4 mg/cm² in front of the target. The plunger device including target and degrader foils was

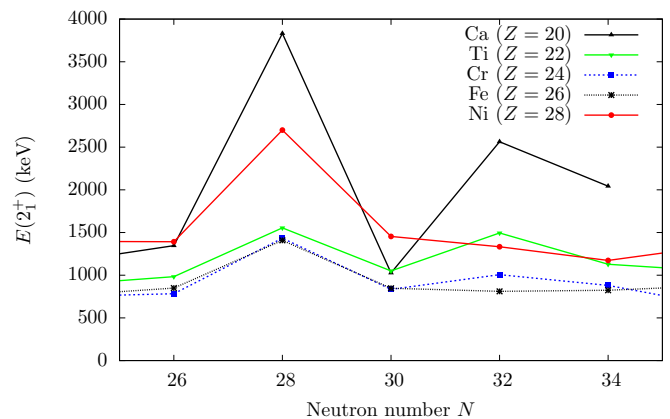


FIG. 1. Evolution of experimental excitation energies $E(2_1^+)$ in neutron-rich even-even Ca-Ni nuclei with $20 \leq Z \leq 28$ and $26 \leq N \leq 34$.

placed close to the grazing angle of the multinucleon-transfer reactions of interest at an angle of 45° with respect to the beam axis. Target and degrader foils were mounted orthogonal to the entrance axis of the magnetic spectrometer VAMOS++ [24–26]. The ^{50}Ti target layer had an effective thickness of $\approx 2.1 \text{ mg/cm}^2$ resulting in an effective ^{238}U beam energy of 6.16 MeV/u in the middle of the ^{50}Ti layer, taking into account the energy loss in the Cu layer with an effective thickness of $\approx 0.57 \text{ mg/cm}^2$. A $^{\text{nat}}\text{Mg}$ degrader foil with a thickness of $\approx 3.2 \text{ mg/cm}^2$ was placed downstream the target. The targetlike recoils were thus slowed down before entering the VAMOS++ magnetic spectrometer, consisting of two quadrupoles, a dipole magnet, and an array of focal plane detectors, for an event-by-event particle identification. A schematic drawing of the experimental setup is shown in Fig. 1 of Ref. [27] (without the EXOGAM detectors). The focal plane detection system was used to identify the mass (A), charge (Q) and atomic number (Z) of the reaction products. It consisted of a multiwire proportional counter (MWPC), four drift chambers and a segmented ionization chamber. The dual position-sensitive multiwire proportional counter (DPS-MWPC) [26] placed at the entrance of the spectrometer provided the start signal for the time-of-flight (TOF) and the position (x, y) of the recoiling reaction products. Together with the MWPC at the focal plane, they provide the TOF and the direction of the velocity of the ions for Doppler correction. The drift chambers, which also detected the position (x, y) as well as the emission angles (θ, ϕ) of the recoiling reaction products, were used together with the DPS-MWPC to determine the trajectory of the ions after the dipole magnet. Finally, the ionization chamber was employed for measuring the total energy E and energy loss ΔE of the ions at the focal plane. In the present experiment, the magnetic field of the VAMOS++ dipole was set such that a magnetic rigidity of $B\rho = 0.975 \text{ Tm}$ was selected for the central trajectory in the spectrometer.

Prompt γ rays were detected by the Advanced Gamma Tracking Array (AGATA) [28,29]. At the time of this experiment, it consisted of 29 36-fold encapsulated germanium detectors in ten cryostats placed at a radial distance of $\approx 23.5 \text{ cm}$ to the target center and covered angles from 120° – 175° with respect to the optical axis of the spectrometer. Using the velocity vector reconstructed by VAMOS++ and the position of the first γ -ray interaction in AGATA, the observed γ rays were Doppler corrected on an event-by-event basis using the angle between the scattered particle and the direction of γ rays detected in AGATA. The γ -ray interaction points, determined by the pulse shape analysis (PSA) using GRID search algorithm techniques [30], were tracked by using the Orsay forward tracking (OFT) algorithm [31]. The particle velocity after passing through the degrader foil is used for the Doppler correction. Therefore, the slow component, corresponding to photon emissions after the degrader, occurs at the nominal γ -ray energy whereas the fast component is shifted toward lower energies, as AGATA was located at backward angles.

Data were taken at six different nominal target-to-degrader distances between $70 \mu\text{m}$ and $1000 \mu\text{m}$ for about 24 h per distance, which results in sensitivity to lifetimes ranging from a few ps to about 400 ps.

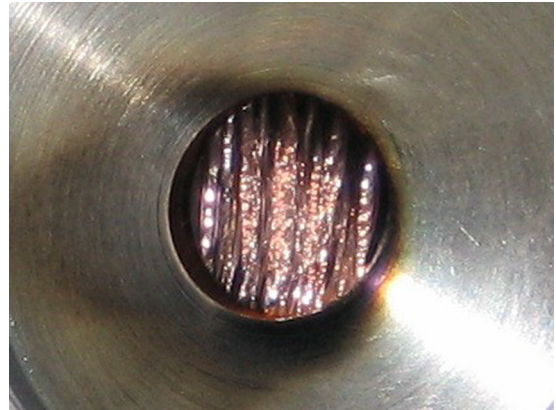


FIG. 2. Beam-induced changes observed for the ^{50}Ti plunger target. The originally stretched target foil was severely damaged. Here, the side of the target with the copper layer that was facing the beam.

A. Target degradation and effective plunger distances

During the experiment, despite the low beam current of 0.1 pA , beam-induced changes of the ^{50}Ti target occurred, even though estimates of the beam spot temperature from the momentum transfer of the beam did not indicate any significant thermal load. A self-supporting ^{50}Ti target with a thickness of $\approx 1.5 \text{ mg/cm}^2$ was used at first. This target developed wrinklelike structures with amplitudes of about $100 \mu\text{m}$ soon after being exposed to the 6.76 MeV/u ^{238}U beam with a beam current of 0.1 pA . To improve heat conductivity, this target was replaced by the aforementioned $\approx 1.5 \text{ mg/cm}^2$ ^{50}Ti target with an additional $\approx 0.4 \text{ mg/cm}^2$ copper that was evaporated onto the ^{50}Ti foil. The copper layer was facing the beam. This target experienced similar damages after being exposed to the beam (see Fig. 2). Nevertheless, as no other alternative was available, the ^{50}Ti target with the additional copper layer was used. After a careful analysis, the observed degradation of the target can be explained as resulting from the sensitivity of the Ti material to the electronic stopping of heavy ions (see Ref. [32]). This effect leads to a drastic increment of the lattice temperature of Ti induced by the irradiation by the highly energetic ^{238}U ions (so-called thermal spikes) and thus to structural damages of the Ti target foil. Titanium is very sensitive to this effect due to its large Debye temperature on the one hand and its low thermal conductivity on the other hand. This observation can be reproduced within the thermal-spike model (see, e.g., Ref. [33]). The degrader, on the other hand, showed no such effects since magnesium has a much lower Debye temperature and a higher thermal conductivity.

For this reason, a direct and precise determination of the distances between the plunger target and the degrader was not possible. Instead, average absolute distances for each distance setting need to be specified as the structural changes to target continue to take place during the ^{238}U beam exposure. These distances are referred to as the effective distances and can be extracted from γ -ray spectra related to nuclear states whose lifetimes are known with high precision. A strongly populated reaction channel produced ^{46}Ti (see Fig. 3 for the corresponding spectrum), for which a high-precision RDDS

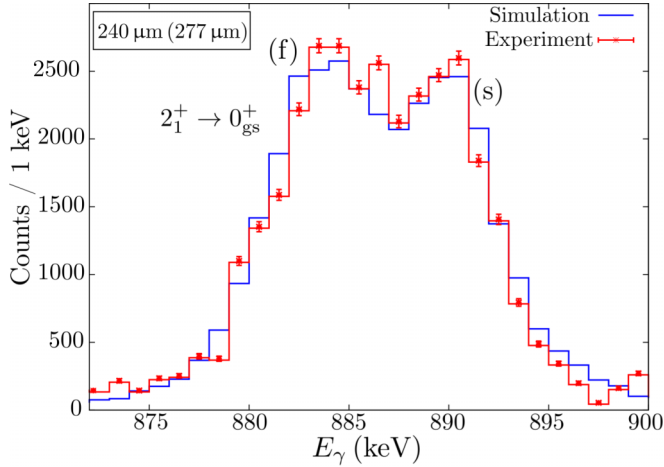


FIG. 3. Experimental (red) and simulated (blue) γ -ray energy spectra of ^{46}Ti at an effective target-to-degrader distance of $277\ \mu\text{m}$, Doppler corrected for the degraded component. The fast (f) and slow (s) components are also labeled. See text for details.

measurement was performed only recently with results published in Ref. [34]. Since ^{46}Ti isotopes were produced via multinucleon-transfer reactions, only the low-lying states 2_1^+ , 4_1^+ , and 6_1^+ were populated, so that other feeding can be excluded. Feeding corrections for the observed transitions from the 4^+ and 6^+ states were taken into account in the analysis.

For the determination of effective distances, γ -ray spectra for ^{46}Ti were created through a versatile GEANT4-based Monte Carlo simulation tool [35] using a precise experimental geometry including that for the target chamber and the AGATA detectors. For the distance determination, distance assumptions were provided to the simulation toolkit and their values were varied in discrete steps. For illustration, Fig. 3 shows a representative comparison of the experimental spectra showing the $2_1^+ \rightarrow 0_{\text{gs}}^+$ transition in ^{46}Ti at a nominal distance of $240\ \mu\text{m}$ with the best-fitting simulation, assuming a separation following the described approach. For each comparison between the simulated and the experimental spectrum, a χ^2 value was calculated according to the following modified version of the least-squares method:

$$\chi^2 = \sum_i \left(\frac{i_{\text{exp}} - i_{\text{sim}}}{\Delta i_{\text{exp}}} \right)^2,$$

where i_{exp} (i_{sim}) is the number of counts in bin i in the experimental (simulated) spectrum. The chosen range was restricted to both the fast and slow components of the considered transition. An example of this approach with the χ^2 method is depicted in Fig. 4 for the nominal distance of $300\ \mu\text{m}$. A similarly good description using the χ^2 method can be observed for the other distances. The statistical uncertainty is extracted from distance values at $\chi_{\text{min}}^2 + 1$ (cf. Fig. 4). Table I shows the effective distances d resulting from the individual ^{46}Ti simulations.

The velocities of the recoil ions were determined as follows: the velocity after the degrader was measured directly by VAMOS++, whereas the velocity between target and

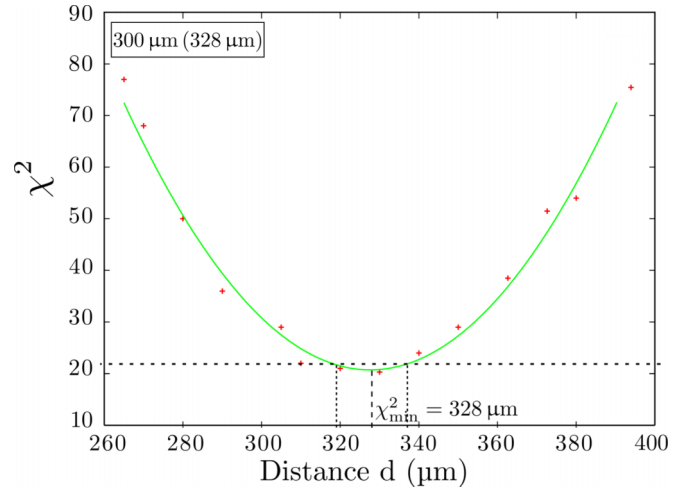


FIG. 4. Determination of the mean distance using the standard χ^2 method for a nominal distance of $300\ \mu\text{m}$. As indicated, the errors of the χ^2 method are deduced from lifetimes with $\chi_{\text{min}}^2 + 1$. See text for details.

degrader was deduced from the experimentally observed Doppler shift between the two components of the transitions. The mean recoil velocity behind the target (degrader) is $\beta_D = 12.70(21)\%$ [$\beta_D = 11.68(23)\%$] of the speed of light.

III. DATA ANALYSIS AND RESULTS

Figure 5(a) shows the energy loss ΔE versus the total energy E spectra, using which the recoils with specific atomic number Z can be identified. The mass-over-charge A/Q ratio and the mass A are determined from the TOF, the path through the spectrometer, and the magnetic rigidity. The mass resolution for the isotopic chains, shown in Fig. 5(b), was $\frac{\Delta M}{M} \approx 1.4\%$, so that an unambiguous identification of the reaction residues in the mass region around $A = 50$ was possible.

Figure 6 shows the γ -ray spectra after Doppler correction with $\beta_D = 11.68\%$ for the slow component detected with AGATA in coincidence with ^{54}Ti and ^{52}Ti ions identified in VAMOS++, summed over all six distances. Therefore, the slow component appears at nominal γ -ray energy while the fast component has lower energy. It can be clearly seen that the statistics for ^{52}Ti is ≈ 13 times higher than that for ^{54}Ti .

TABLE I. Effective distances d resulting from a comparison with the simulations and corresponding nominal distances d_{exp} used for the measurement (i.e., relative to electrical contact at the start of the experiment).

$d_{\text{exp}}\ (\mu\text{m})$	$d\ (\mu\text{m})$
70	102(8)
150	198(9)
180	200(6)
240	277(10)
300	328(9)

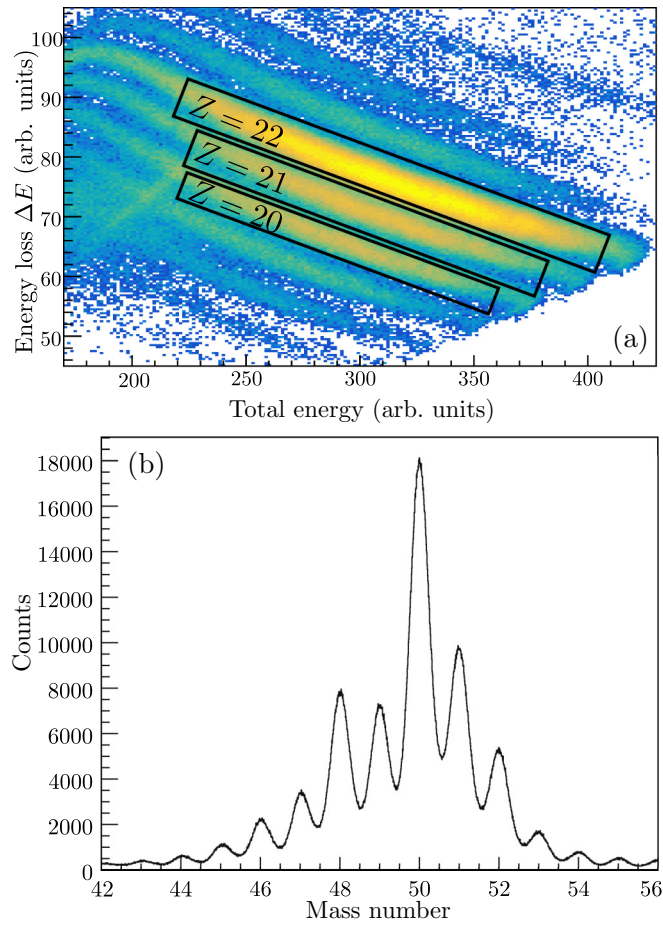


FIG. 5. (a) Energy loss of the targetlike reaction products in VAMOS++ as a function of total detected energy. The isotopes of titanium ($Z = 22$), scandium ($Z = 21$), and calcium ($Z = 20$) are marked schematically with black rectangles. (b) Mass spectrum showing resolution for the titanium isotopic chain.

The clearly visible variations of the intensities of the fast and slow components with the distance d in the Doppler-corrected energy spectra for the $2_1^+ \rightarrow 0_{\text{gs}}^+$ transition in ^{54}Ti at three different distances are shown in Fig. 7. During the fitting procedure, the peak positions and widths were fixed. The latter were determined by calibrating the line width using the γ -ray spectra of $^{50,52,53}\text{Ti}$, which have a significantly higher level of statistics than that of ^{54}Ti . Due to the relatively small difference in the velocity of $\Delta v = 0.0102c$, the fast and slow components of the γ -ray lines are not well separated from each other.

Lifetimes of the excited states in $^{52,54}\text{Ti}$ were extracted from the γ -ray intensities for each distance in the sensitive range (see Eq. (20) in Ref. [23]) using the differential decay curve method (DDCM) [36]. The lifetime of an excited state should not depend on the target-to-degrader distances at which it has been determined, therefore, τ values are expected to remain unchanged with plunger distance. In ^{54}Ti it is possible to identify five transitions: $2_1^+ \rightarrow 0_{\text{gs}}^+$ (1495 keV), $4_1^+ \rightarrow 2_1^+$ (1002 keV), $6_1^+ \rightarrow 4_1^+$ (439 keV), $8_1^+ \rightarrow 6_1^+$ (2523 keV), and a transition at 840 keV from a state with unknown spin and

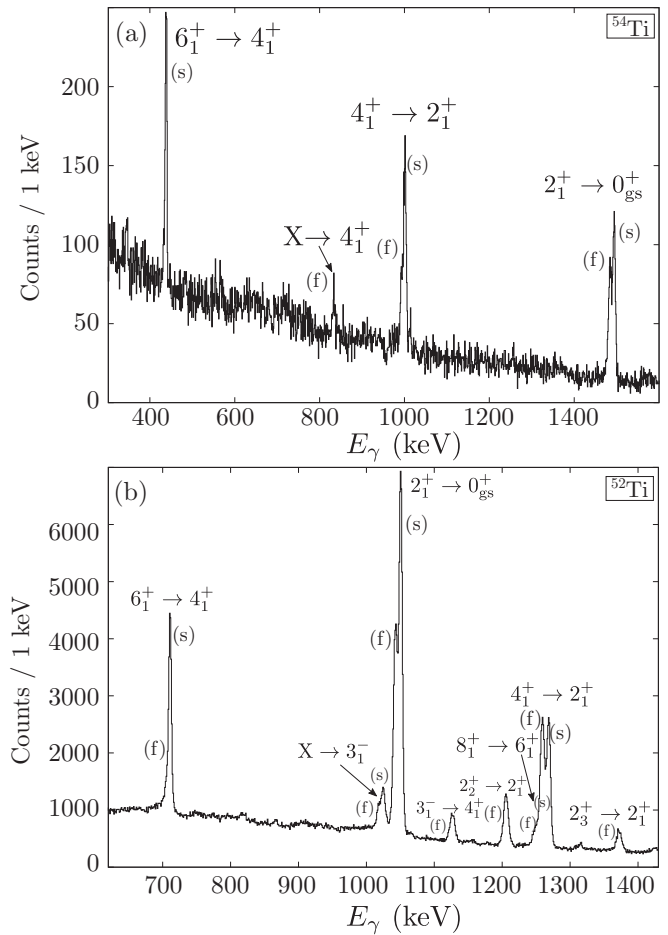


FIG. 6. γ -ray spectra in coincidence with ions identified as ^{54}Ti (a) and ^{52}Ti (b), summed over all six distances. In this energy range four (eight) γ -ray decays are visible in ^{54}Ti (^{52}Ti). The fast (f) and slow (s) components are labeled.

parity J^π deexciting to the 4_1^+ state. Only for the $2_1^+ \rightarrow 0_{\text{gs}}^+$ and $4_1^+ \rightarrow 2_1^+$ transitions both components are visible for all distances. For the 439 keV $6_1^+ \rightarrow 4_1^+$ transition, only the slow component is visible at all distances. Therefore, only a lower limit of the 6_1^+ lifetime could be determined. In contrast, for the 840 keV $8_1^+ \rightarrow 6_1^+$ transition at 2523 keV only the fast component is visible at all distances, and as a consequence only an upper limit of the 8_1^+ lifetime was deduced. In ^{52}Ti it is possible to identify ten transitions: $2_1^+ \rightarrow 0_{\text{gs}}^+$ (1050 keV), $4_1^+ \rightarrow 2_1^+$ (1268 keV), $6_1^+ \rightarrow 4_1^+$ (711 keV), $8_1^+ \rightarrow 6_1^+$ (1258 keV), $2_2^+ \rightarrow 2_1^+$ (1214 keV), $2_3^+ \rightarrow 2_1^+$ (1382 keV), $3_1^- \rightarrow 4_1^+$ (1135 keV), $(10_1^+) \rightarrow 8_1^+$ (2406 keV), $10_2^+ \rightarrow 8_1^+$ (3232 keV), and $J^\pi \rightarrow 3_1^-$ (1025 keV). It should be noted that the γ -ray spectra are particle-gated singles spectra. For the lifetime determination of the 2_1^+ , 4_1^+ , 6_1^+ , and 8_1^+ states, a feeding correction was carried out by subtracting the intensities of the slow component of a direct feeder from the intensity of the slow component of γ decay of the state to be analyzed. All contributions from states outside the yrast band have been neglected due to nonobserved slow components, which means that these states are characterized by a rather small lifetime. It should be

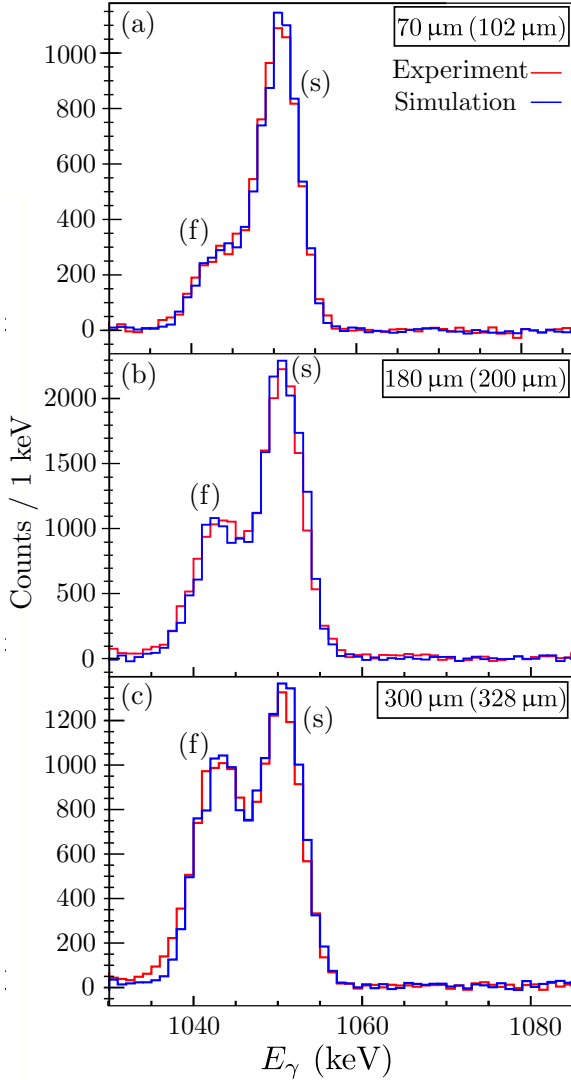


FIG. 7. Simulated (blue) and experimental (red) particle-gated singles γ -ray energy spectra showing the $2_1^+ \rightarrow 0_{\text{gs}}^+$ transition at 1050 keV in ^{52}Ti at three target-to-degrader distances at backward angles. The development of intensity ratios of the fast (f) and slow (s) components with increasing distances is clearly visible.

mentioned that the fast component of the $4_1^+ \rightarrow 2_1^+$ transition is equal in energy to the slow component of the $8_1^+ \rightarrow 6_1^+$ transition. In order to account for this, an intensity function depending on the spin was first established by determining the intensities of the fast and slow components of the $2_1^+ \rightarrow 0_{\text{gs}}^+$, $6_1^+ \rightarrow 4_1^+$, and $10_2^+ \rightarrow 8_1^+$ transitions in ^{52}Ti in the spectrum summed up over all distances. This intensity function was compared to the corresponding one in ^{48}Ti , this is possible due to similarity of the level schemes. Using the intensity function, in the sum spectrum the added intensities ($I_{f+s,\text{sum}}(J_1^+ \rightarrow (J-2)_1^+)$) of the fast and slow components of the $4_1^+ \rightarrow 2_1^+$ and $8_1^+ \rightarrow 6_1^+$ transitions in ^{52}Ti were calculated. Then the intensities of the $2_1^+ \rightarrow 0_{\text{gs}}^+$ transitions were determined for each distance ($I_{f+s,\text{dist}}(2_1^+ \rightarrow 0_{\text{gs}}^+)$) and the unknown intensities of the $4_1^+ \rightarrow 2_1^+$ and $8_1^+ \rightarrow 6_1^+$ were calculated accord-

ing to $I_{f+s,\text{dist}}(J_1^+ \rightarrow (J-2)_1^+) = \alpha_i \cdot I_{f+s,\text{dist}}(2_1^+ \rightarrow 0_{\text{gs}}^+)$ with $\alpha_i = \frac{I_{f+s,\text{sum}}(J_1^+ \rightarrow (J-2)_1^+)}{I_{f+s,\text{sum}}(2_1^+ \rightarrow 0_{\text{gs}}^+)}$, with $I_{f+s,\text{sum}}(2_1^+ \rightarrow 0_{\text{gs}}^+)$ is the added intensity of the fast and slow components of the $2_1^+ \rightarrow 0_{\text{gs}}^+$ transition in the sum spectrum. The relevant plots for the lifetime analysis for the decay of the 2_1^+ and 4_1^+ states in ^{54}Ti (^{52}Ti) are shown in Fig. 8 (Fig. 9). Fits of the intensities of the two components were performed with the NAPATAU code [39]. Here a feeding correction was carried out so that the summed intensity of I_s and I_f does not have to be constant. The different plot curves of the intensity of the slow components of Figs. 8 and 9 result from the different slopes in the intensities of the fast components. The weighted average lifetime is calculated using the points inside the region of sensitivity, i.e., from the maximum of the slope of the decay curve to its half value. The weighted averages of the mean lifetimes in $^{52,54}\text{Ti}$ are summarized along with the corresponding $E2$ transition strengths in Table II. The statistical uncertainty of each lifetime value is dominated by the distribution of the individual τ values. The uncertainty of the recoil velocity and the uncertainty of the relative target-to-degrader distances have dominant contributions to the systematic errors of the lifetime. The final experimental error of the lifetime results from the root sum squared of the statistical and the systematic uncertainties.

In addition, the lifetimes determined according to DDCM were verified with the GEANT4-based Monte Carlo tool. Figure 7 shows a comparison between the experimental and simulated γ -ray spectra for ^{52}Ti at three different distances.

The lifetime $\tau(2_1^+) = 1.3(5)$ ps of the 2_1^+ state in ^{54}Ti determined in this work corresponds to a reduced transition probability of $B(E2; 2_1^+ \rightarrow 0_{\text{gs}}^+) = 84_{-23}^{+53} e^2\text{fm}^4$ and agrees with the adopted lifetime $\tau(2_1^+) = 1.53(27)$ ps with corresponding $B(E2; 2_1^+ \rightarrow 0_{\text{gs}}^+) = 72_{-11}^{+15} e^2\text{fm}^4$ [9] within their error limits.

In ^{52}Ti there is a considerable discrepancy between the new $B(E2; J_1^+ \rightarrow (J-2)_1^+)$ values in this work for 2_1^+ , 4_1^+ , 6_1^+ yrast states and the previously measured $B(E2)$ values [37,38] (see Fig. 13). The lifetime values of the 2_1^+ and 4_1^+ states from Ref. [37] and this measurement differ by a factor of approximately 2.

IV. DISCUSSION

A. Systematics

The results of this work yield new insights into the shell evolution for neutron-rich Ti, Cr, and Fe isotopes. Figure 10 illustrates the systematics of excitation energies and the evolution of $B(E2; 2_1^+ \rightarrow 0_{\text{gs}}^+)$ values for even-even nuclei with $20 \leq Z \leq 28$ and $26 \leq N \leq 34$. The $B(E2; 2_1^+ \rightarrow 0_{\text{gs}}^+)$ value in ^{52}Ti has been obtained in the present work, that for ^{54}Ti is taken from Ref. [9] (being consistent with the present result but subject to a smaller uncertainty), and the remaining values are adopted ones [40]. At the neutron shell closure $N = 28$, all depicted isotopes are characterized by high excitation energies of the first 2_1^+ state and relatively small $B(E2; 2_1^+ \rightarrow 0_{\text{gs}}^+)$ values (see Fig. 10). At $N = 30$ all isotones show a reduction of the 2_1^+ energies, but the $B(E2; 2_1^+ \rightarrow 0_{\text{gs}}^+)$ values exhibit a

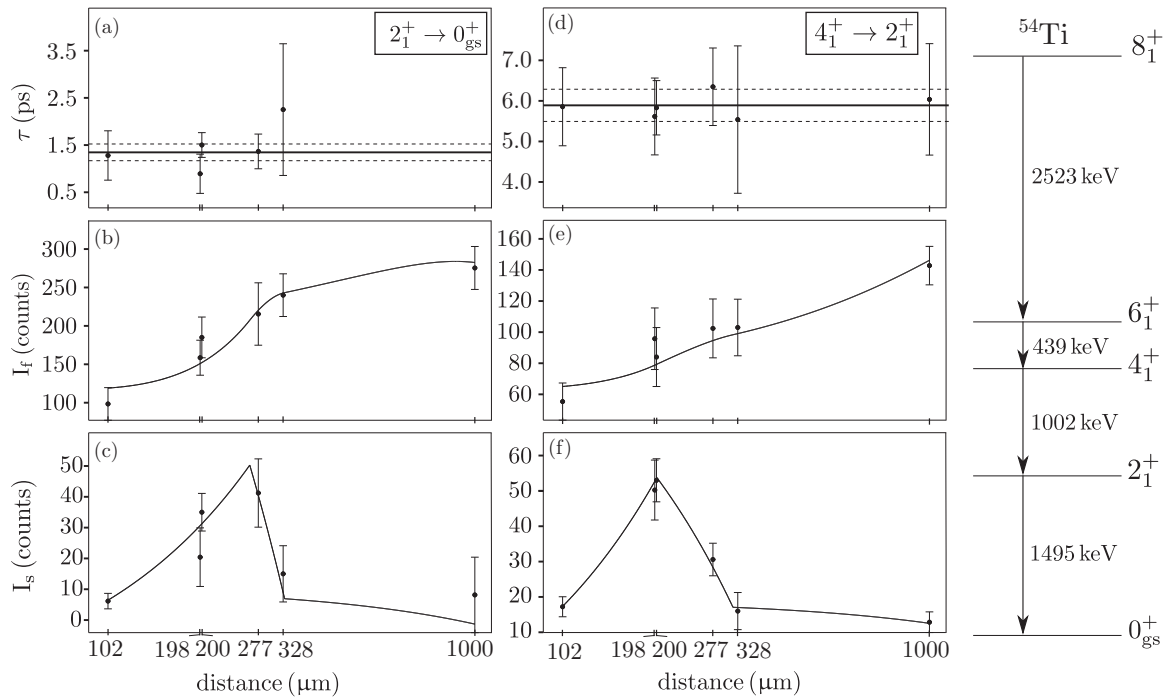


FIG. 8. Lifetime curves (a), (d) for the 2_1^+ (left) and 4_1^+ (middle) states in ^{54}Ti . Black solid lines in (a), (d) represent the weighted mean value of the lifetime; dashed lines mark the statistical uncertainty. In addition, the intensities of the fast (b), (e) and slow (c), (f) components are shown, where the latter are corrected for delayed observed feeding. The polynomial fit function to the intensities is presented in solid black in (b), (e) and (c), (f). Note the logarithmic distance scale. Right: Partial level scheme with the relevant γ -ray transitions in the yrast band in ^{54}Ti .

clear increase with the only exception case of ^{50}Ca . The newly measured value for ^{52}Ti indicates only a shallow increase compared to the neighboring values and fits nicely into the isotonic evolution.

Increasing the neutron number by two and four, the behavior of the 2_1^+ energies of Ca isotopes at $N = 32, 34$ is attributed to the local $\nu 2p_{3/2}$ and $\nu 2p_{1/2}$ subshell closures as discussed in Refs. [14,20]. Figure 11 shows the relevant

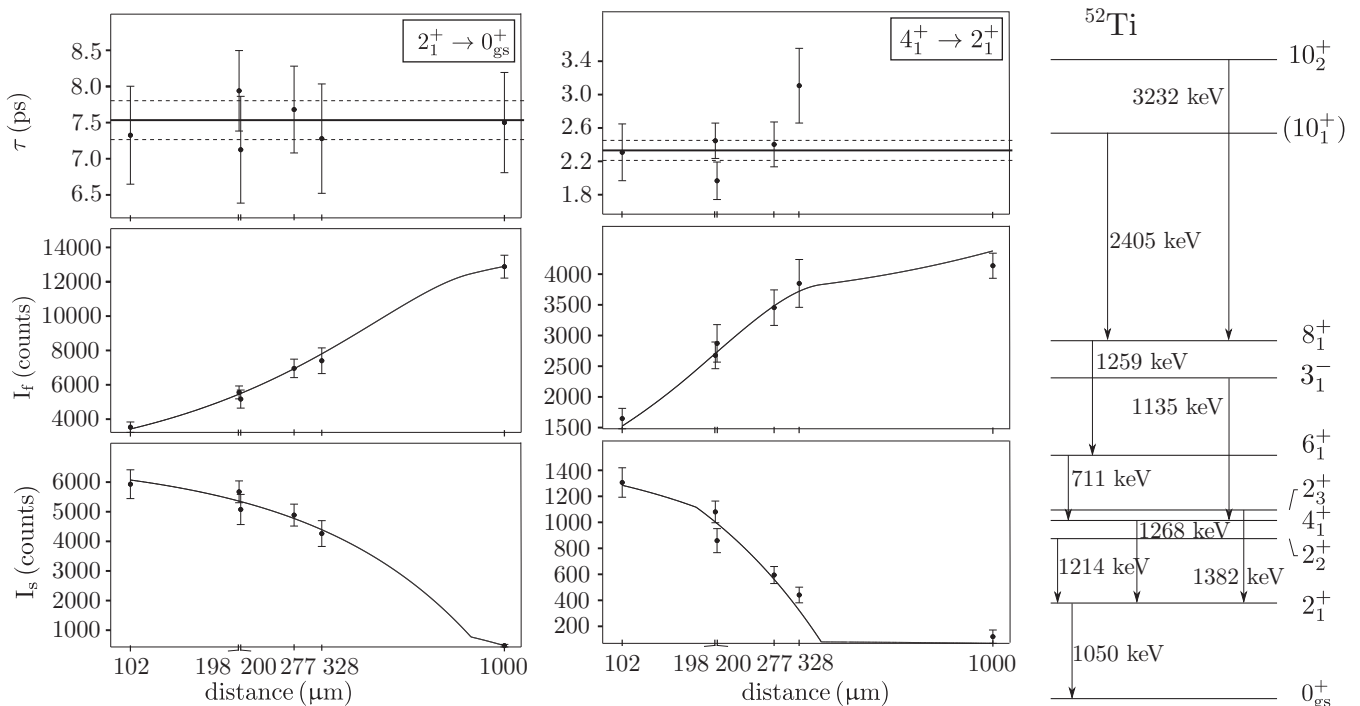


FIG. 9. Same as Fig. 8 for ^{52}Ti .

TABLE II. Lifetime values for the first four yrast states in $^{52,54}\text{Ti}$ obtained in the present experiment compared to previous experimental values taken from Refs. [9,37,38]. The corresponding experimental $B(E2; J_1^+ \rightarrow (J-2)_1^+)$ values are presented as well.

Nucleus	^{52}Ti				^{54}Ti			
	Lifetime (ps)		$B(E2)$ ($e^2\text{fm}^4$)		Lifetime (ps)		$B(E2)$ ($e^2\text{fm}^4$)	
	This work	Previous	This work	Previous	This work	Previous	This work	Previous
2_1^+	7.5(4)	5.19(20) [37]	86_{-4}^{+5}	124_{-5}^{+5} [37]	1.3(5)	1.53(27) [9]	84_{-23}^{+53}	72_{-11}^{+15} [9]
4_1^+	2.3(3)	4.76(58) [37]	109_{-13}^{+16}	53_{-6}^{+7} [37]	5.9(9)	–	139_{-18}^{+25}	–
6_1^+	45.0(31)	36.7(63) [38]	100_{-6}^{+7}	123_{-18}^{+25} [38]	≥ 380	–	≤ 132	–
8_1^+	29.4(21)	–	8.8_{-1}^{+1}	–	≤ 1.4	–	≥ 5.7	–

neutron orbitals above $N = 28$ are $\nu 2p_{3/2}$, $\nu 1f_{5/2}$, and $\nu 2p_{1/2}$. In most of the known nuclei close to stability, the $\nu 1f_{5/2}$ orbital is energetically close to $\nu 2p_{3/2}$. Therefore, no $N = 32$ shell closure is observed as shown on the left of Fig. 11 [9,42]. As the number of protons in the $\pi 1f_{7/2}$ orbital are decreased, i.e., from nickel to calcium, the $\nu 1f_{5/2}$ orbital becomes less bound, and at $^{52}\text{Ca}_{32}$ the order of the $\nu 1f_{5/2}$ and $\nu 2p_{1/2}$ orbitals becomes inverted [14,20]. The raising of the $\nu 1f_{5/2}$ orbital produces a gap between the lower-lying $\nu 2p_{3/2}$ and the higher-lying $\nu 1f_{5/2}$ and $\nu 2p_{1/2}$ orbitals. This leads to the local $N = 32$ subshell closure (see right side of Fig. 11) and the higher 2_1^+ energy in ^{52}Ca [14,16]. Thus, the phase transition

from predominantly collective structures in ^{60}Ni to a neutron subshell closure at ^{52}Ca can be attributed to the weakening of the attractive proton-neutron interaction between the $\pi 1f_{7/2}$ and $\nu 1f_{5/2}$ orbitals with decreasing number of protons in the $\pi 1f_{7/2}$ orbital [14,20].

Figure 10 shows that in the case of the Ti isotopes, a similar peaking of 2_1^+ energy is observed at $N = 32$ as for the Ca isotopes, although with a reduced amplitude, while for Cr this effect is much weaker and for Fe and Ni completely disappears. This speaks for the existence of a reduced $N = 32$ subshell closure in the Ti isotopes, which has recently been confirmed in mass measurements [42]. The systematics of $B(E2; 2_1^+ \rightarrow 0_{\text{gs}}^+)$ values in Ti isotopes obtained in earlier experiments showed a staggering anticorrelated with the subshell closures at $N = 28$ and $N = 32$. The revised $B(E2; 2_1^+ \rightarrow 0_{\text{gs}}^+)$ value in ^{52}Ti reduces the amplitude of this staggering. The underlying nuclear structure of the lowest yrast states and $E2$ strengths can be addressed in the framework of the nuclear shell model.

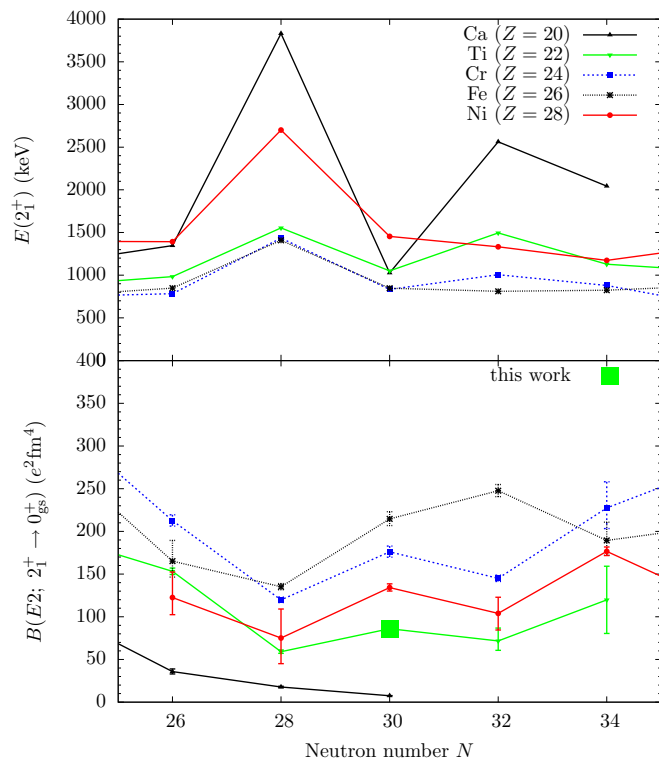


FIG. 10. Systematics of excitation energies for the 2_1^+ state (top) and the evolution of the $B(E2; 2_1^+ \rightarrow 0_{\text{gs}}^+)$ (bottom) values in even-even nuclei with $20 \leq Z \leq 28$ and $26 \leq N \leq 34$ including the result for ^{52}Ti obtained in the present work. For ^{54}Ti the result from Ref. [9] is shown due to its smaller uncertainty.

B. Comparison with shell-model calculations

In the present work, shell-model calculations were performed with the code NUSHELLX@MSU [43] using three interactions, namely, KB3G [44], GXPF1A [45], and GXPF1B [46]. The model space comprises the full pf main shell, coupled to a ^{40}Ca core. Effective charges $e_\pi = 1.31e$ and $e_\nu = 0.46e$ were used for protons and neutrons, respectively, for all interactions [47]. The choice of the neutron effective

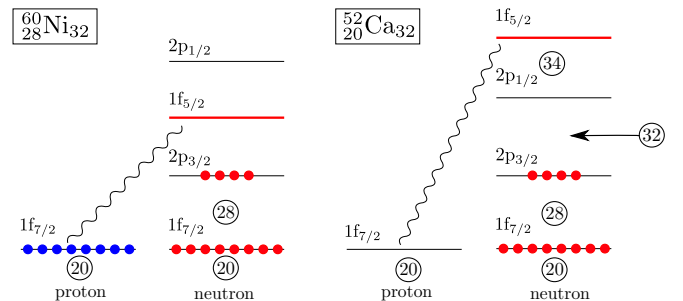


FIG. 11. Schematic illustration of shell evolution from Ni to Ca for neutron orbits. The wavy line represents the interaction between the proton in the $1f_{7/2}$ orbit and the neutron in the $1f_{5/2}$ orbit. See text for more details. Adopted from Ref. [41].

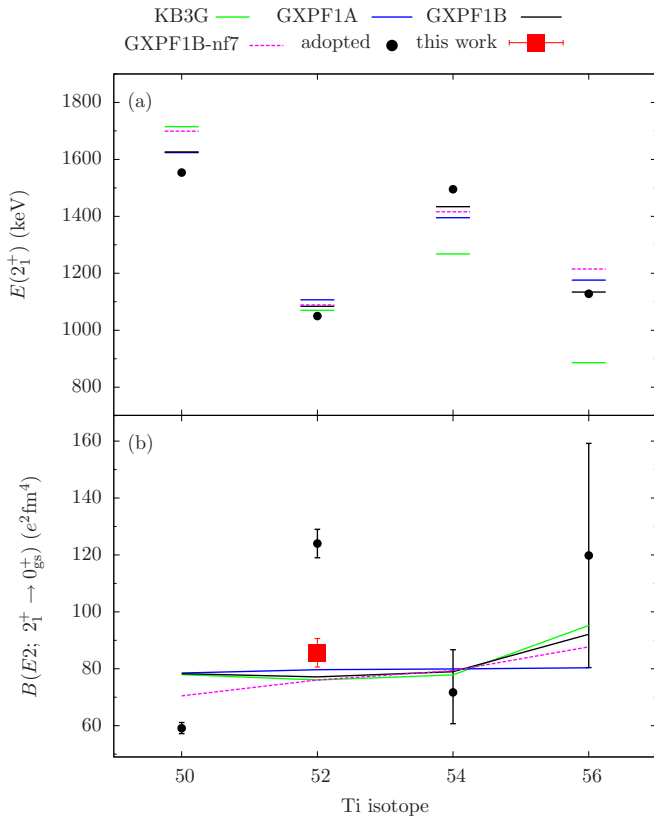


FIG. 12. Comparison of experimental 2_1^+ excitation energies (a) and $B(E2; 2_1^+ \rightarrow 0_{\text{gs}}^+)$ transition strengths (b) with the results of shell-model calculations using the KB3G, GXPF1A, GXPF1B, and GXPF1B-nf7 interactions for $^{50-56}\text{Ti}$.

charge is justified for the neighboring isotopes with $N > 28$ [48], while the microscopically justified proton effective charge [47] has an intermediate value between the standard isoscalar $e_\pi = 1.5e$ value and the value of $e_\pi = 1.15e$, which is suggested to be more adequate for the $\pi 1f_{7/2}$ orbital and especially for the $N = Z$ region [49].

Figure 12 shows a comparison of experimental and shell-model systematics of the 2_1^+ energies and the $B(E2; 2_1^+ \rightarrow 0_{\text{gs}}^+)$ values for $^{50-56}\text{Ti}$. The excitation energies are listed in

Table III. All used interactions describe the experimental excitation energies reasonably well.

As seen in Fig. 12 the previously adopted values displayed a staggering in the $B(E2; 2_1^+ \rightarrow 0_{\text{gs}}^+)$ values, which has been a topic of several works. Although the established interactions were able to describe the excitations energies in these Ti isotopes and the structure of the neighboring nuclei, they were generally unable to exactly reproduce the staggering in the experimental $B(E2; 2_1^+ \rightarrow 0_{\text{gs}}^+)$ values in neutron-rich Ti isotopes using isoscalar proton and neutron effective charges [9,48,50]. As can be seen from Fig. 12, the new $B(E2; 2_1^+ \rightarrow 0_{\text{gs}}^+)$ systematics for $^{50-54}\text{Ti}$ exhibits a clearly weaker staggering with a rather flat behavior around $N = 30$ and similar values. A splitting in the $B(E2; 2_1^+ \rightarrow 0_{\text{gs}}^+)$ trends becomes apparent for ^{56}Ti , where the values obtained using GXPF1A and GXPF1B interactions differ clearly from each other, with the latter one showing an increased value closer to the experimental result. Since the GXPF1B interaction was optimized to describe the local subshell closure at $N = 34$ in ^{54}Ca [46], it is not surprising that it also reproduces the isotone ^{56}Ti better than GXPF1A. The KB3G interaction yields a similar good description for $^{52-56}\text{Ti}$. Regarding ^{50}Ti ($N = 28$), there is clear overprediction of the $B(E2; 2_1^+ \rightarrow 0_{\text{gs}}^+)$ values by all shell-model interactions. One possible explanation is that proton particle-hole excitations across the $Z = 20$ ^{40}Ca core are present in the 0_{gs}^+ state and, to a lesser extent, in the 2_1^+ state, which are not accounted for in this model space, leading to an overprediction of the $E2$ strength. Another explanation is given by the inspection of the wave function of the 0_{gs}^+ and 2_1^+ states in ^{50}Ti in the GXPF1A (GXPF1B) calculations, which each predict about 30% (for the 0_{gs}^+) and 38% (for the 2_1^+) configurations with neutron particle-hole excitations across the $N = 28$ shell, which increase the specific $B(E2; 2_1^+ \rightarrow 0_{\text{gs}}^+)$ strength. Therefore, to reduce the $E2$ strength from neutron $N = 28$ cross-shell excitations, an ad hoc modification of the GXPF1B interaction was introduced, called GXPF1B-nf7, where the single-particle energy of the $\nu 1f_{7/2}$ orbital was lowered by 1 MeV. The results for GXPF1B-nf7 are presented in Figs. 12, 13, and Table III) and compared to the experimental values and those calculated using other interactions. This interaction has only a qualitative value, but may be relevant for $^{50-52}\text{Ti}$ and generally provides the best results for the $^{50-56}\text{Ti}$ $B(E2; 2_1^+ \rightarrow 0_{\text{gs}}^+)$ systematics. The transition

TABLE III. Experimental excitation energies for the 2_1^+ , 4_1^+ , and 6_1^+ states in $^{50,52,54,56}\text{Ti}$ compared to those resulting from shell-model calculations using GXPF1A, GXPF1B, GXPF1B-nf7, and KB3G interactions. For a better comparison the root-mean-square deviation (*RMSD*) for each interaction is provided.

	Excitation energy E (keV)												<i>RMSD</i>
	^{50}Ti			^{52}Ti			^{54}Ti			^{56}Ti			
	2_1^+	4_1^+	6_1^+	2_1^+	4_1^+	6_1^+	2_1^+	4_1^+	6_1^+	2_1^+	4_1^+	6_1^+	
Experiment	1553	2675	3199	1050	2318	3029	1495	2496	2936	1128	2288	2978	–
GXPF1A	1624	2562	3237	1106	2251	2932	1395	2465	2975	1176	2278	2868	72.6
GXPF1B	1626	2568	3234	1084	2239	2922	1434	2476	2974	1134	2296	2873	66.8
GXPF1B-nf7	1699	2572	3153	1089	2229	2899	1416	2468	2965	1215	2312	2900	82.9
KB3G	1715	2841	3383	1069	2356	3048	1285	2452	3048	886	1995	2873	159.1

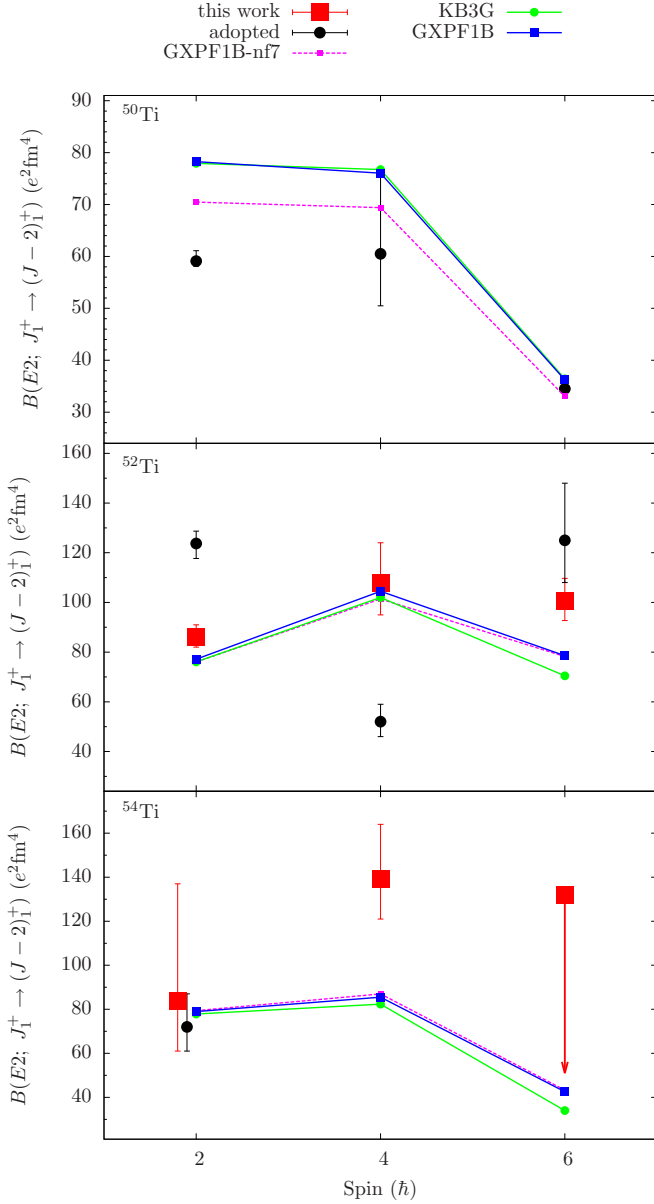


FIG. 13. Comparison of experimental $B(E2; J_1^+ \rightarrow (J-2)_1^+)$ values in $^{50,52,54}\text{Ti}$ with the results of the shell-model calculations with different effective interactions. See text for details.

strengths in the calculations are computed as $B(E2; J_1^+ \rightarrow (J-2)_1^+) = (A_p e_\pi + A_n e_\nu)^2 / (2J_1 + 1)$ [51]. Here, A_p and A_n (in units of fm^2) are the proton and neutron amplitudes and are summarized in Table IV for the $2_1^+ \rightarrow 0_{\text{gs}}^+$ transitions in $^{50-56}\text{Ti}$ for four different interactions. Small A_n are characteristic of shell gaps at $N = 28$ and $N = 32$, as discussed in Ref. [9].

In conclusion, the general flat trends in the $B(E2; 2_1^+ \rightarrow 0_{\text{gs}}^+)$ values of the shell model can be understood as resulting from a fine balance of proton and neutron amplitudes. Specifically, the variation in the $B(E2; 2_1^+ \rightarrow 0_{\text{gs}}^+)$ values due to A_n is nearly canceled by that due to A_p , leading to constant $B(E2; 2_1^+ \rightarrow 0_{\text{gs}}^+)$ values calculated using these effective charges. Thus, regarding the systematics of the lowest transi-

TABLE IV. Proton and neutron amplitudes for the $2_1^+ \rightarrow 0_{\text{gs}}^+$ of four different interactions for even-even $^{50-56}\text{Ti}$. See text for more details.

$2_1^+ \rightarrow 0_{\text{gs}}^+$	^{50}Ti		^{52}Ti		^{54}Ti		^{56}Ti	
	A_p	A_n	A_p	A_n	A_p	A_n	A_p	A_n
GXPF1A	11.59	10.06	9.96	15.17	11.54	10.62	11.02	12.21
GXPF1B	11.58	10.01	9.66	15.19	11.72	9.81	11.31	14.43
GXPF1B-nf7	11.83	7.12	9.84	14.36	11.76	9.82	11.72	12.16
KB3G	11.87	9.21	9.37	15.70	10.76	12.24	10.30	18.09

tion strengths, a consistent picture between experimental and theoretical results emerges.

In the following, the properties of the higher-spin states in the even $^{50-54}\text{Ti}$ are discussed. As the trends between GXPF1A and GXPF1B for these isotopes are similar, only the results using the GXPF1B interaction are discussed below. Figure 13 shows a comparison between the experimental results and the shell-model calculations for the $B(E2; J_1^+ \rightarrow (J-2)_1^+)$ values.

For ^{50}Ti , the experimental $B(E2; 2_1^+ \rightarrow 0_{\text{gs}}^+)$ value from Ref. [52] is slightly lower than that estimated by the present calculations, independent of the interaction. As already mentioned above, this could be attributed to either the proton particle-hole excitations across the $Z = 20$ ^{40}Ca core present in the 0_{gs}^+ state, which are not accounted for in this model space, or, as discussed above, the $B(E2)$ value could be overestimated due to the degree of neutron particle-hole excitation across $N = 28$ as qualitatively demonstrated by the calculation using the GXPF1B-nf7 interaction. The adopted $B(E2; 4_1^+ \rightarrow 2_1^+)$ and $B(E2; 6_1^+ \rightarrow 4_1^+)$ values agree well (within 2σ) with the theoretical predictions for all interactions. The shell-model calculations predict that the 2_1^+ , 4_1^+ , 6_1^+ states in ^{50}Ti have a proton character dominated in $\geq 70\%$ by configurations of the type $\pi_{J^+} \otimes \nu_{0^+}$.

For the neighboring nucleus ^{52}Ti , the predictions generally agree well with the new $B(E2)$ values (see Fig. 13). Only the $B(E2; 2_1^+ \rightarrow 0_{\text{gs}}^+)$ and $B(E2; 6_1^+ \rightarrow 4_1^+)$ values are slightly overestimated or underestimated. In contrast to ^{50}Ti , the wave function of the 2_1^+ state has a dominant neutron character with $\approx 50\%$ $\pi_{0^+} \otimes \nu_{2^+}$ and $\approx 30\%$ $\pi_{2^+} \otimes \nu_{0^+}$ configuration. The two neutrons above $N = 28$ occupy predominantly the $2p_{3/2}$ orbital in which they can couple to a maximum angular momentum of $2\hbar$. Therefore, the higher-spin 4_1^+ , 6_1^+ yrast states cannot be of pure neutron character. For the 4_1^+ state, mixed proton-neutron configurations $\approx 30\%$ $\pi_{2^+} \otimes \nu_{2^+}$ and $\approx 40\%$ $\pi_{4^+} \otimes \nu_{0^+}$ prevail for KB3G and GXPF1B. The wave functions of the three interactions are similar for the case of the 6_1^+ state. The configuration $\pi_{6^+} \otimes \nu_{0^+}$ has the largest contribution to the wave function ($\leq 50\%$), followed by the mixed configurations of type $\pi_{4^+} \otimes \nu_{2^+}$ and $\pi_{6^+} \otimes \nu_{2^+}$ ($\leq 12\%$). We note the very good agreement between the new experimental $B(E2)$ values from the present work and the theory both having the opposite trend as a function of spin to the adopted data from Refs. [37,38]. The new results are free of the longstanding contradiction between the shell model and

adopted $B(E2; 2_1^+ \rightarrow 0_{\text{gs}}^+)$ in ^{52}Ti , thus putting in doubt the previous experimental results.

For ^{54}Ti , i.e., four neutrons above $N = 28$, all interactions reproduce fairly accurately the $B(E2; 2_1^+ \rightarrow 0_{\text{gs}}^+)$ value from Ref. [9] and yield very similar $B(E2; 4_1^+ \rightarrow 2_1^+)$ values. However, the predicted values are clearly lower than $B(E2; 4_1^+ \rightarrow 2_1^+) = 139_{-18}^{+25} e^2\text{fm}^4$ determined in the present work. For the $6_1^+ \rightarrow 4_1^+$ transition, the calculations yield $B(E2)$ values half the size of those for the $4_1^+ \rightarrow 2_1^+$ and $2_1^+ \rightarrow 0_{\text{gs}}^+$ transitions. From our data, we have an upper limit of $B(E2; 6_1^+ \rightarrow 4_1^+) \leq 132 e^2\text{fm}^4$, which agrees with the calculations. In addition, the experimental lower limit of $B(E2; 8_1^+ \rightarrow 6_1^+) \geq 5.7 e^2\text{fm}^4$ agrees with $7.0 e^2\text{fm}^4$ calculated using the GXPF1B interaction. The wave functions calculated using the KB3G and GXPF1B interactions show a distinct proton occupation as found in the case of ^{50}Ti . For the 2_1^+ state, the proton occupation yields $\approx 50\% \pi_{2+} \otimes \nu_{0+}$ corresponding to a subshell closure of $\nu 2p_{3/2}$. This confirms that the $p_{3/2}$ and $f_{5/2}$ orbitals are not close to each other. Also the other higher-lying states $J = 4_1^+, 6_1^+$ show a clear proton character ($\approx 60\% \pi_{4+} \otimes \nu_{0+}$ and $\geq 70\% \pi_{6+} \otimes \nu_{0+}$ for both KB3G and GXPF1B interactions). The trend in the predicted $B(E2; J_1^+ \rightarrow (J-2)_1^+)$ values resembles with that for ^{50}Ti , which is another signature of the $N = 32$ subshell closure.

V. SUMMARY

The structure of the neutron-rich nuclei $^{52,54}\text{Ti}$ produced via multinucleon-transfer reactions in inverse kinematics was investigated. The lifetime of the 2_1^+ state in ^{54}Ti was remeasured. The transition probability obtained from the measured lifetime of the 2_1^+ state is in agreement with that from an earlier Coulomb-excitation work [9]. The lifetime of the 4_1^+

state in ^{54}Ti , a lower limit for the 6_1^+ state, and an upper limit for the 8_1^+ state were determined for the first time.

The comparison with shell-model calculations shows the following outcome: In ^{54}Ti the trend of the $B(E2; J_1^+ \rightarrow (J-2)_1^+)$ values agrees well with the results of shell-model calculations using various interactions, only the experimental result of the $B(E2; 4_1^+ \rightarrow 2_1^+)$ value is underestimated.

In ^{52}Ti , the lifetimes of the $2_1^+, 4_1^+$, and 6_1^+ states were remeasured with a surprising result. The transition probabilities obtained from the lifetimes determined in this work show an opposite trend with spin to the literature $B(E2; J_1^+ \rightarrow (J-2)_1^+)$ values [37,38]. The $B(E2; 2_1^+ \rightarrow 0_{\text{gs}}^+)$ value obtained in the present work is smaller than the adopted value. A similar behavior was noted for the $6_1^+ \rightarrow 4_1^+$ transition strength. While, the new $B(E2; 4_1^+ \rightarrow 2_1^+)$ value is larger than the adopted value. In contrast to the previously adopted results for ^{52}Ti , the new results on $B(E2; J_1^+ \rightarrow (J-2)_1^+)$ values are well reproduced within the shell model. Compared to those for the neighboring isotopes, the new $B(E2; 2_1^+ \rightarrow 0_{\text{gs}}^+)$ results reduce the amplitude of the staggering along the titanium isotopic chain $^{50-54}\text{Ti}$. The experimental and theoretical results confirm a subshell closure at $N = 32$ in ^{54}Ti that is somewhat weaker compared to that at $N = 28$.

ACKNOWLEDGMENTS

We thank the GANIL team for the professional support during the experiment. The research leading to these results has received funding from the German BMBF under Contract No. 05P18PKFN9 and partially supported by Generalitat Valenciana, Conselleria d'Educació, Investigació, Cultura i Esport under the grant PROMETEU/2019/005 and Ministerio de Ciencia, Innovación y Universidades Spain, under grants SEV-2014-0398 and FPA2017-84756-C4 and by the European Commission FEDER funds.

-
- [1] B. A. Brown, *Prog. Part. Nucl. Phys.* **47**, 517 (2001).
- [2] T. Braunroth, A. Dewald, H. Iwasaki, S. M. Lenzi, M. Albers, V. M. Bader, T. Baugher, T. Baumann, D. Bazin, J. S. Berryman *et al.*, *Phys. Rev. C* **92**, 034306 (2015).
- [3] A. Gade, R. V. F. Janssens, T. Baugher, D. Bazin, B. A. Brown, M. P. Carpenter, C. J. Chiara, A. N. Deacon, S. J. Freeman, G. F. Grinyer *et al.*, *Phys. Rev. C* **81**, 051304(R) (2010).
- [4] S. M. Lenzi, F. Nowacki, A. Poves, and K. Sieja, *Phys. Rev. C* **82**, 054301 (2010).
- [5] C. Santamaria, C. Louchart, A. Obertelli, V. Werner, P. Doornenbal, F. Nowacki, G. Authalet, H. Baba, D. Calvet, F. Château *et al.*, *Phys. Rev. Lett.* **115**, 192501 (2015).
- [6] W. Rother, A. Dewald, H. Iwasaki, S. M. Lenzi, K. Starosta, D. Bazin, T. Baugher, B. A. Brown, H. L. Crawford, C. Fransen *et al.*, *Phys. Rev. Lett.* **106**, 022502 (2011).
- [7] J. Ljungvall, A. Gorgen, A. Obertelli, W. Korten, E. Clement, G. deFrance, A. Burger, J. P. Delaroche, A. Dewald, A. Gadea, L. Gaudefroy, M. Girod, M. Hackstein, J. Libert, D. Mengoni, F. Nowacki, T. Pissulla, A. Poves, F. Recchia, M. Rejmund, W. Rother, E. Sahin, C. Schmitt, A. Shrivastava, K. Sieja, J. Valiente-Dobon, K. O. Zell, and M. Zielinska, *Phys. Rev. C* **81**, 061301(R) (2010).
- [8] H. L. Crawford, R. M. Clark, P. Fallon, A. O. Macchiavelli, T. Baugher, D. Bazin, C. W. Beausang, J. S. Berryman, D. L. Bleuel, C. M. Campbell *et al.*, *Phys. Rev. Lett.* **110**, 242701 (2013).
- [9] D. C. Dinca, R. V. F. Janssens, A. Gade, D. Bazin, R. Broda, B. A. Brown, C. M. Campbell, M. P. Carpenter, P. Chowdhury, J. M. Cook, A. N. Deacon, B. Fornal, S. J. Freeman, T. Glasmacher, M. Honma, F. G. Kondev, J. L. Lecouey, S. N. Liddick, P. F. Mantica, W. F. Mueller, H. Olliver, T. Otsuka, J. R. Terry, B. A. Tomlin, and K. Yoneda, *Phys. Rev. C* **71**, 041302(R) (2005).
- [10] H. Hübel, A. Bürger, T. R. Saito, H. Grawe, P. Reiter, J. Gerl, M. Görška, H. J. Wollersheim, A. Al-Khatib, A. Banu *et al.*, *Acta Physica Hungarica A) Heavy Ion Physics* **25**, 197 (2006).
- [11] M. Seidlitz, P. Reiter, A. Dewald, O. Möller, B. Bruyneel, S. Christen, F. Finke, C. Fransen, M. Görška, H. Grawe *et al.*, *Phys. Rev. C* **84**, 034318 (2011).

- [12] M. J. LeVine, E. K. Warburton, and D. Schwalm, *Phys. Rev. C* **23**, 244 (1981).
- [13] O. Kenn, K.-H. Speidel, R. Ernst, J. Gerber, P. Maier-Komor, and F. Nowacki, *Phys. Rev. C* **63**, 064306 (2001).
- [14] D. Steppenbeck, S. Takeuchi, N. Aoi, P. Doornenbal, M. Matsushita, H. Wang, H. Baba, N. Fukuda, S. Go, M. Honma *et al.*, *Nature (London)* **502**, 207 (2013).
- [15] J. I. Prisciandaro, P. F. Mantica, B. A. Brown, D. W. Anthony, M. W. Cooper, A. Garcia, D. E. Groh, A. Komives, W. Kumarasiri, P. A. Lofy *et al.*, *Phys. Lett. B* **510**, 17 (2001).
- [16] A. Huck, G. Klotz, A. Knipper, C. Miehe, C. Richard-Serre, G. Walter, A. Poves, H. L. Ravn, and G. Marguier, *Phys. Rev. C* **31**, 2226 (1985).
- [17] R. V. F. Janssens, B. Fornal, P. F. Mantica, B. A. Brown, R. Broda, P. Bhattacharyya, M. P. Carpenter, M. Cinausero, P. J. Daly, A. D. Davies *et al.*, *Phys. Lett. B* **546**, 55 (2002).
- [18] B. Fornal, S. Zhu, R. V. F. Janssens, M. Honma, R. Broda, P. F. Mantica, B. A. Brown, M. P. Carpenter, P. J. Daly, S. J. Freeman *et al.*, *Phys. Rev. C* **70**, 064304 (2004).
- [19] S. N. Liddick, P. F. Mantica, R. Broda, B. A. Brown, M. P. Carpenter, A. D. Davies, B. Fornal, T. Glasmacher, D. E. Groh, M. Honma *et al.*, *Phys. Rev. C* **70**, 064303 (2004).
- [20] T. Otsuka, T. Suzuki, R. Fujimoto, H. Grawe, and Y. Akaishi, *Phys. Rev. Lett.* **95**, 232502 (2005).
- [21] T. Otsuka, R. Fujimoto, Y. Utsuno, B. A. Brown, M. Honma, and T. Mizusaki, *Phys. Rev. Lett.* **87**, 082502 (2001).
- [22] T. Otsuka, T. Suzuki, M. Honma, Y. Utsuno, N. Tsunoda, K. Tsukiyama, and M. Hjorth-Jensen, *Phys. Rev. Lett.* **104**, 012501 (2010).
- [23] A. Dewald, O. Möller, and P. Petkov, *Prog. Part. Nucl. Phys.* **67**, 786 (2012).
- [24] S. Pullanhiotan, M. Rejmund, A. Navin, W. Mittig, and S. Bhattacharyya, *Nucl. Instrum. Methods Phys. Res., Sect. A* **593**, 343 (2008).
- [25] M. Rejmund, B. Lecornu, A. Navin, C. Schmitt, S. Damoy, O. Delaune, J. M. Enguerrand, G. Fremont, P. Gangnant, L. Gaudefroy *et al.*, *Nucl. Instrum. Methods Phys. Res., Sect. A* **646**, 184 (2011).
- [26] M. Vandebrouck, A. Lemasson, M. Rejmund, G. Fremont, J. Pancin, A. Navin, C. Michelagnoli, J. Goupil, C. Spitaels, and B. Jacquot, *Nucl. Instrum. Methods Phys. Res. A* **812**, 112 (2016).
- [27] Y. H. Kim, A. Lemasson, M. Rejmund, A. Navin, S. Biswas, C. Michelagnoli, I. Stefan, R. Banik, P. Bednarczyk, S. Bhattacharyya *et al.*, *Eur. Phys. J. A* **53**, 162 (2017).
- [28] S. Akkoyun, A. Algora, B. Alikhani, F. Ameil, G. de Angelis, L. Arnold, A. Astier, A. Ataç, Y. Aubert, C. Aufranc *et al.*, *Nucl. Instrum. Methods Phys. Res. A* **668**, 26 (2012).
- [29] E. Clément, C. Michelagnoli, G. de France, H. Li, A. Lemasson, C. B. Dejean, M. Beuzard, P. Bougault, J. Cacitti, J.-L. Foucher *et al.*, *Nucl. Instrum. Methods Phys. Res. A* **855**, 1 (2017).
- [30] R. Venturelli and D. Bazzacco, LNL Annual Report 2004 (2005), p. 220.
- [31] A. Lopez-Martens, K. Hauschild, A. Korichi, J. Roccas, and J.-P. Thibaud, *Nucl. Instrum. Methods Phys. Res. A* **533**, 454 (2004).
- [32] Z. G. Wang, C. Dufour, E. Paumier, and M. Toulemonde, *J. Phys.: Condens. Matter* **6**, 6733 (1994).
- [33] M. Toulemonde, E. Paumier, and C. Dufour, *Radiat. Eff. Defects Solids* **126**, 201 (1993).
- [34] A. Goldkuhle, C. Fransen, A. Dewald, K. Arnsward, M. Bast, M. Beckers, A. Blazhev, T. Braunroth, G. Hackenberg, G. Häfner *et al.*, *Eur. Phys. J. A* **55**, 53 (2019).
- [35] T. Braunroth (private communication).
- [36] A. Dewald, S. Harissopulos, and P. von Brentano, *Z. Phys. A Atomic Nuclei* **334**, 163 (1989).
- [37] K.-H. Speidel, J. Leske, S. Schielke, S. C. Bedi, O. Zell, P. Maier-Komor, S. J. Q. Robinson, Y. Y. Sharon, and L. Zamick, *Phys. Lett. B* **633**, 219 (2006).
- [38] B. A. Brown, D. B. Fossan, A. R. Poletti, and E. K. Warburton, *Phys. Rev. C* **14**, 1016 (1976).
- [39] B. Saha, Computer code NAPATAU, 2002.
- [40] ENSDF database, 2019.
- [41] T. Otsuka and Y. Tsunoda, *J. Phys. G: Nucl. Part. Phys.* **43**, 024009 (2016).
- [42] E. Leistenschneider, M. P. Reiter, S. Ayet San Andrés, B. Kootte, J. D. Holt, P. Navrátil, C. Babcock, C. Barbieri, B. R. Barquest, J. Bergmann *et al.*, *Phys. Rev. Lett.* **120**, 062503 (2018).
- [43] B. Brown and W. Rae, *Nucl. Data Sheets* **120**, 115 (2014).
- [44] A. Poves, J. Sánchez-Solano, E. Caurier, and F. Nowacki, *Nucl. Phys. A* **694**, 157 (2001).
- [45] M. Honma, T. Otsuka, B. A. Brown, and T. Mizusaki, *Eur. Phys. J. A - Hadrons and Nuclei* **25**, 499 (2005).
- [46] M. Honma, T. Otsuka, and T. Mizusaki, RIKEN Accel. Prog. Rep. **41**, 32 (2008).
- [47] M. Dufour and A. P. Zuker, *Phys. Rev. C* **54**, 1641 (1996).
- [48] J. J. Valiente-Dobón, D. Mengoni, A. Gadea, E. Farnea, S. M. Lenzi, S. Lunardi, A. Dewald, T. Pissulla, S. Szilner, R. Broda *et al.*, *Phys. Rev. Lett.* **102**, 242502 (2009).
- [49] R. du Rietz, J. Ekman, D. Rudolph, C. Fahlander, A. Dewald, O. Möller, B. Saha, M. Axiotis, M. A. Bentley, C. Chandler *et al.*, *Phys. Rev. Lett.* **93**, 222501 (2004).
- [50] A. Poves, F. Nowacki, and E. Caurier, *Phys. Rev. C* **72**, 047302 (2005).
- [51] B. Brown, A. Arima, and J. McGrory, *Nucl. Phys. A* **277**, 77 (1977).
- [52] S. Raman, C. Nestor, and P. Tikkanen, *At. Data Nucl. Data Tables* **78**, 1 (2001).